COMMUNICATIONS CHEMISTRY

ARTICLE

https://doi.org/10.1038/s42004-019-0157-9 OPEN

Measuring ion-pairing and hydration in variable charge supramolecular cages with microwave microfluidics

Angela C. Stelson [1], Cynthia M. Hong [2,3], Mitchell C. Groenenboom[4], Charles A.E. Little[1], James C. Booth[1], Nathan D. Orloff[1], Robert G. Bergman[2,3], Kenneth N. Raymond[2,3], Kathleen A. Schwarz[4], F. Dean Toste [2,3] & Christian J. Long[1]

Metal-organic supramolecular cages can act as charged molecular containers that mediate reactions, mimic enzymatic catalysis, and selectively sequester chemicals. The hydration of these cages plays a crucial role in their interactions with other species. Here we use microwave microfluidics to measure the hydration and ion pairing of two metal-organic cage assemblies that are isostructural but have different overall anionic charge. We supplement our measurements with density functional theory calculations to compare binding site energies on model metal-organic cage vertices. We find that the cage with dianionic vertices is more strongly hydrated and forms a distinct ion pair species from the cage with trianionic vertices. We evaluate multi-ion species and distinct ion pair solvations as possible sources for differences in ion dynamics and hydration. Broadly, this work highlights the utility of microwave microfluidics to elucidate the consequences of charge states on metal-organic complexes in solution.

[1] Communications Technology Laboratory, National Institute of Standards and Technology, 325 Broadway, Boulder, CO 80305, USA. [2] Chemical Sciences Division, Lawrence Berkeley National Laboratory, Berkeley, CA 94720, USA. [3] Department of Chemistry, University of California, Berkeley, CA 94720, USA. [4] Materials Measurement Laboratory, National Institute of Standards and Technology, 100 Bureau Dr., Gaithersburg, MD 20899, USA. Correspondence and requests for materials should be addressed to A.C.S. (email: angela.stelson@nist.gov)

Cavity-bearing supramolecular cages offer unprecedented opportunities for chemical control at the molecular level. These structures feature internal microenvironments that recognize and encapsulate molecular guests, act as enzyme-mimetic catalysts, and unlock new modes of reactivity[1]. A common design motif for such supramolecular catalysts are self-assembled metal–organic cages that consist of organic ligands coordinating cationic metal ions to generate a variety of charged, polyhedral architectures. These cages are commonly identified by the counterions, metal vertex atoms, and ligands (e.g., $K_{12}Ga_4L_6$) that describe the overall stoichiometry and charge of the system (see Fig. 1a as an example).

The reactivities of supramolecular catalysts are influenced by parameters, such as cavity size, overall charge, and solvent exclusion. However, the impact of dynamics in solution on reactivity is largely not characterized[2–4]. Poorly understood issues include the distribution of charge throughout these supramolecular systems, as well as the localization and rates of ion-pairing interactions[5–9]. These factors are often ignored in the design of supramolecular cages because they are not well understood, despite the fact that they have consequences for chemical applications[4,6,10]. Quantifying interactions between cages, solvent, and counterions would clarify the role that solvation and counterions play in guest association/dissociation and catalysis. Furthermore, pairing measurements with computational models could extend the rational design of cages beyond geometric and architectural considerations of the cage itself to include non-covalent solvent and ion interactions[11].

The challenge for synthetic chemists is that noncovalent interactions (e.g., Coulombic, hydrogen bonding, and solvophobic effects) in solution are difficult to measure directly with traditional analytical chemistry techniques. Some solvation and ionic interactions in metal–organic cage systems were indirectly investigated by combining independent measurement techniques, such as isothermal calorimetry (ITC), nuclear magnetic resonance (NMR) spectroscopy, and ultraviolet/visible spectroscopy[12–16]. However, measurements of counterion interactions remain scarce, and indirect measurements are limited to strong ionic interactions in solution and specific counterion chemistries[17].

Previous microwave (0.1 GHz to 100 GHz) dielectric spectroscopy studies of salt solutions have characterized the solvent-mediated ion pairing and hydration of ions in solution[18–20]. Bulk-fluid dielectric spectroscopy can also measure hydration and ionic interactions in complex biomolecular systems including proteins,

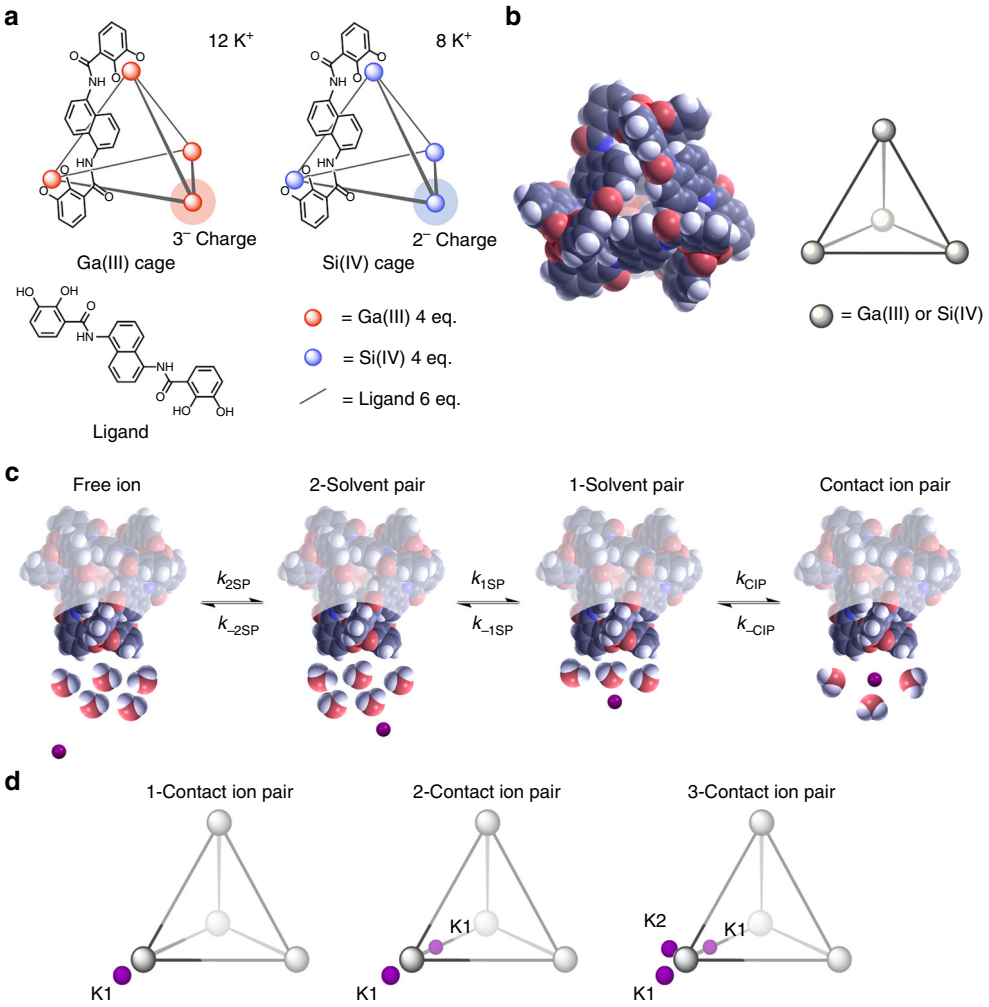

Fig. 1 Schematic representations and the crystal structure. Schematic representation of isostructural metal–organic cages $K_{12}(Ga_4L_6)$ and $K_8(Si_4L_6)$ with one ligand of six shown for clarity. **a** A representative crystal structure of the cages with a schematic shown in the same orientation. **b** Stepwise formation of close contact ion pairs via freely solvated potassium cations, 2-solvent pairing, and 1-solvent pairing of potassium cations at each cage vertex. **c** Schematic representation of stepwise ion-pair formation on the vertex charge center of the cage. Reaction rates for each step are labeled. **d** Schematic representation of different contact ion-pair configurations on the vertex charge center of the cage filling position K1 (1-contact ion pair), K1 equivalent position (2-contact ion pair), and K2 (3-contact ion pair, only considered for the $K_{12}(Ga_4L_6)$ case)

DNA, and cells[21–23]. Microwave–microfluidic measurements enable on-chip measurements for nanoliter fluid volumes over a wide frequency range (0.4 MHz–100 GHz). These measurements quantify the dipolar interactions of cages and their counterions in solution, as well as changes to the cooperative water relaxation and the hydration of cages and counterions[24].

Here, we investigate the ion pairing and hydration of $K_{12}(Ga_4L_6)$ and $K_8(Si_4L_6)$ metal–organic cages (Fig. 1a) with microwave microfluidics. Both structures are tetrahedral with six organic ligands (L = N,N′-bis(2,3-dihydroxybenzoyl)-1,5-diaminonaphthalene) acting as struts to link four cationic metal vertices (Ga(III) and Si(IV)) (Fig. 1b)[2]. These two cage systems are isostructural, but in comparison with $K_{12}(Ga_4L_6)$, each vertex of $K_8(Si_4L_6)$ has its charge reduced from trianionic (Ga(III)-triscatecholates) to dianionic (Si(IV)-triscatecholates). This chemistry lowers the overall anionic charge and potassium counterion number for each host from 12 to 8 for the $K_{12}(Ga_4L_6)$ and $K_8(Si_4L_6)$ cages, respectively. The structural similarity of the cages affords the unique opportunity to not only study the solution-phase dynamics of each cage but also to isolate the impact of varied overall charge on the cage dynamics and ion-pair formation (Fig. 1c, d). Here, we consider multiple solvation states for ion pairs (Fig. 1c) and multiple ions on each vertex (Fig. 1d) as possible ion-pairing configurations. Taken together, our microwave microfluidic measurements and density-functional theory (DFT) models suggest that the increase in hydration in the $K_8(Si_4L_6)$ cage can be explained by the reduction of ions associated with the charged vertices.

Results

Microwave microfluidics measurements. To characterize the hydration and ion pairing in solution, we used broadband (40 kHz–110 GHz) microwave microfluidic measurements. Microwave microfluidic measurements provide critical advantages in measuring supramolecular systems over traditional dielectric spectroscopy. These advantages include smaller sample volumes and a broader frequency range. The broad frequency range allows microwave microfluidics to accurately correct for both the low-frequency effects associated with the electrical double layer (EDL) at the electrode surface and the high-frequency effects from water relaxation. Ion-pairing measurands are typically small in comparison with these effects, so accurate corrections are critical to capture the ion-pair dynamics in supramolecular systems.

To characterize the ion-pair dynamics, we fit the frequency dependence of the experimentally determined electrical capacitance and conductance with a model that included electrode effects, ion-pairing relaxation, and water relaxation (see Device Fabrication in the Methods section). From these fit parameters, we calculated the association rate of cage–ion-pair formation and the hydration numbers of the cages. We then compared the results to Debye–Hückel theory and found that the metal–organic cages are well described by ion–solution theory in the low-concentration limit when each of the metal vertices of the cage were treated as independent ion-pairing sites[25]. DFT calculations of the charged cage vertices showed that the binding energy for $K_{12}(Ga_4L_6)$ to form a multi-ion complex is similar for the binding energy of a single ion-pair in the $K_8(Si_4L_6)$ cage. Our analysis also shows that the $K_8(Si_4L_6)$ cage is more strongly hydrated than the $K_{12}(Ga_4L_6)$ cage.

We used a microwave microfluidics device (Supplementary Fig. 1) to measure the broadband electrical properties of aqueous solutions of $K_{12}(Ga_4L_6)$ and $K_8(Si_4L_6)$ cages over a range of concentrations. The device consisted of microfluidic channels with integrated coplanar waveguides (CPWs) of varying length. We measured each of these devices (top–down view in Supplementary Fig. 1a) with a vector network analyzer (VNA) with microwave probes to determine the raw complex-scattering parameters (S-parameters)[24]. The S-parameters were calibrated and used to extract the distributed circuit parameters of the transmission line: R_0 and L_0, (resistance and inductance per unit length associated with the metallic conductors) and C_{tot} and G_{tot}, (effective capacitance and conductance of the materials in the gap between the center signal line and the ground planes on either side). We present calibrated fluid data as C_f and G_f, as these quantities are related to the real and imaginary parts of the fluid permittivity (ε' and ε''), respectively:

$$\varepsilon' = (C_f - C_{air})k_{geom} + \varepsilon_0, \quad (1)$$

$$\varepsilon'' = \frac{G_f}{\omega} k_{geom} \quad (2)$$

where C_{air} is the per-unit-length capacitance of an air-filled channel, ε_0 is the permittivity of free space, and k_{geom} is a geometric constant which is determined from device structure. While Eqs. (1) and (2) allow us to convert capacitance C_f and scaled conductance $\frac{G_f}{\omega}$ directly to permittivity values, we used permittivity only to describe intrinsic fluid properties and do not present measured data in terms of permittivity. We used Eqs. (1) and (2) to convert extracted admittance to permittivity after the effects of the EDL that forms on the surface of the electrodes had been accounted for.

We determined the distributed conductance and capacitance of microwave microfluidic devices for room-temperature (25 °C ± 2 °C) measurements of air, de-ionized water (DI water), and a range of concentrations of $K_{12}(Ga_4L_6)$ and $K_8(Si_4L_6)$ metal–organic cages (Fig. 2a–d). The distributed capacitance of the air-loaded microfluidic line remained constant as a function of frequency, while the line loaded with DI water had a larger capacitance at low frequencies and a relaxation (a peak in the conductance paired with a drop in the capacitance) at ~20 GHz. This water relaxation has been commonly observed in aqueous solutions, and was attributed to the cooperative relaxation of water molecules[26,27]. The water relaxation was also present in the aqueous cage solution samples. For the aqueous cage solutions at low frequencies (below 10 MHz), we see an additional peak in the conductance and corresponding drop in the capacitance, which we attribute to the relaxation of the EDL at the surface of our electrodes (Fig. 2)[24,28]. The weak ion-pairing relaxation is approximately two orders of magnitude smaller than the water relaxation, and is not easily visible on this plot. Notably, the broad frequency range afforded by microwave microfluidics is required to measure ion pairing in these cages systems because the ion-pairing relaxations extend below the frequency range typically covered by dielectric spectroscopy studies of ion pairing[18]. To extract the signals associated with each dipole in the fluid, we developed a frequency-dependent circuit model to fit the multiple relaxations across the frequency spectrum (see the Methods section for more detail).

Fitting procedure. To extract physical values from the broadband electrical data, we developed a circuit model to describe the total admittance (inverse of impedance) $Y_{tot} = G_{tot} + i\omega C_{tot}$ of the cages in solution (see Supplementary Fig. 2 for circuit diagram):

$$\frac{1}{Y_{tot}} = \frac{2}{Y_{EDL}} + \frac{1}{Y_f} \quad (3)$$

where Y_{EDL} and Y_f are the admittances of the EDL and fluid, respectively. The model for the EDL is described in detail in the Methods and elsewhere[24]. The fluid admittance can be described

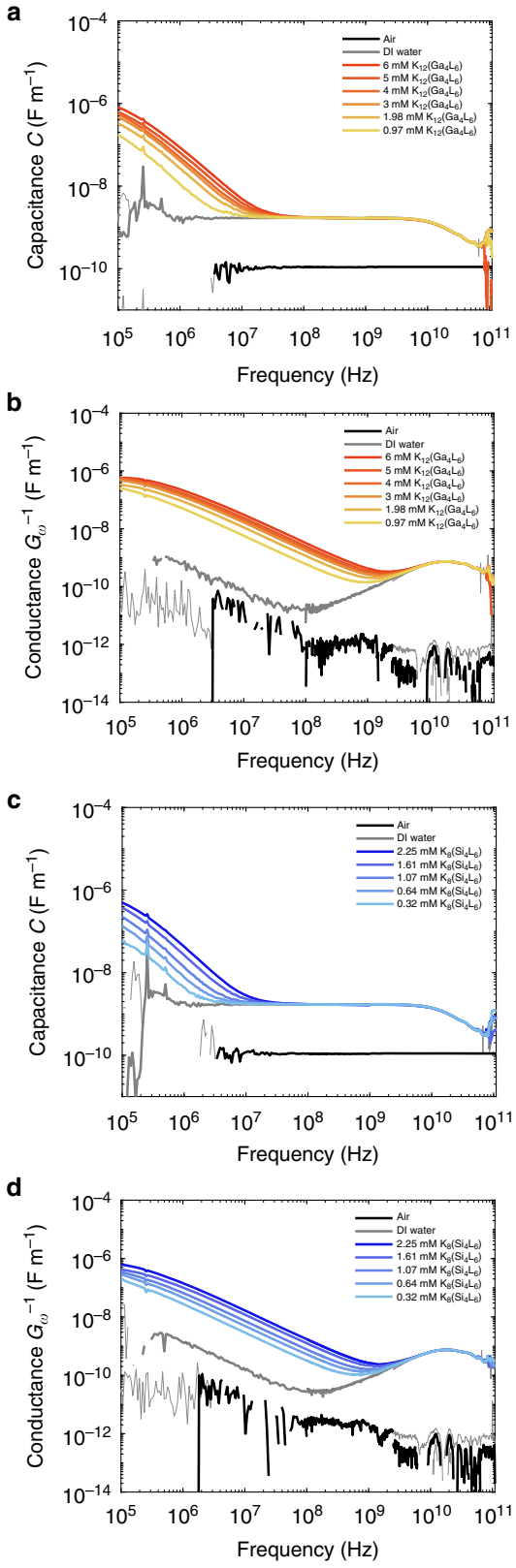

Fig. 2 Microwave measurements of $K_8(Si_4L_6)$ and $K_{12}(Ga_4L_6)$ cages. Calibrated distributed capacitance C_{tot} (**a**, **c**) and distributed conductance $\frac{G_{tot}}{\omega}$ (**b**, **d**) for air, DI water, and a range of concentrations of $K_{12}(Ga_4L_6)$ cages (0.97 mM to 6 mM) (**a**, **b**) $K_8(Si_4L_6)$ cages (0.34 mM to 2.25 mM) and (**c**, **d**)

as four parallel distributed circuit components:

$$Y_f = Y_{IP} + Y_w + G_\sigma + i\omega C_\infty = i\omega\frac{C_{IP}}{1+(i\omega\tau_{IP})} + i\omega\frac{C_w}{1+(i\omega\tau_w)} + G_\sigma + i\omega C_\infty \quad (4)$$

where C_∞ is the capacitance of the suspension at frequencies far above the relaxation of water, C_w is the dipolar contribution of the water, G_σ is the conductance due to cages and counterions, and C_{IP} is the dipolar contribution of the weak ion pairing. The time constants τ_w and τ_{IP} correspond to the relaxation times of the water and the cage-counterion pair, respectively. To fit these responses with Debye models, we performed a nonlinear least-squares fit to extract Y_{tot} (see the Methods section for fit methodology). We plot all extracted physical parameters (C_{IP}, G_σ, etc.) versus the stoichiometric ionic strength I of the solutions:

$$I = \frac{1}{2}\sum[c_i]z_i^2 \quad (5)$$

where c is the molar concentration of the solution. We use the ionic strength to account for the differences in charge distribution in the solutions, and to compare more directly to Debye–Hückel theory of salt solutions. We use the extracted fit parameters for each ionic strength solution to quantify and compare the hydration and ion-pairing dynamics in the two-cage systems.

DFT models of cage vertices. We designed a model system consisting of a single-cage vertex with a truncated ligand to evaluate binding sites for potassium ions and estimate the binding energies of the ion pairs formed by K+ ions and the vertices of the Ga and Si cages. We note that this model does not evaluate types of ion pairing, because it does not include entropic effects and solvent effects, but rather provides a framework to understand the relative charge effects of the cage-vertex environments. We find the lowest energy configurations between the K+ ions, which we designate K1 (two equivalent sites) and K2 (schematic representation in Fig. 1d, molecular model in Supplementary Fig. 3). We note that the equivalent K1 site is located inside the cage cavity, and the steric effects of the cage ligand are not considered in this simplified model, We calculate the DFT energies of contact ion pairs for model cage vertices (Supplementary Table 3) and find that the Ga cage–ion-pairing energies are much larger than those of the Si cage for the K1, K1 equivalent, and K2 positions. The DFT-binding energy with a second potassium added to the K12(Ga4L6) system (i.e., 2-contact ion pair) is energetically comparable with that of a single K1 bound to the K8(Si4L6) cage (i.e., 1-contact ion pair).

Hydration of $K_8(Si_4L_6)$ and $K_{12}(Ga_4L_6)$. The water relaxation at ~20 GHz is affected by the hydration of the cages and counterions. We calculated the apparent number of irrotationally bound (immobilized and not participating in the water relaxation) and displaced solvent molecules Z_{IB}^{ap} from Eq. (6):

$$Z_{IB}^{ap} = \frac{c_s^o - c_s^{ap} - V_{cage} * c}{c} \quad (6)$$

where c_s^o is the analytical concentration of water at 25 °C, c is the concentration of the cages, c_s^{ap} is the apparent concentration of the water, and V_{cage} is the volume of the cage in solution (see the Methods section for calculation)[19,29]. The apparent concentration can be calculated as:

$$c_s^{ap} = \frac{2\varepsilon'(c)+1}{2\varepsilon'(0)+1} \times \frac{\varepsilon'(0)}{\varepsilon'(c)} \times \frac{c_s^o(0)}{C_w(0)} C_w(c) \quad (7)$$

where $\varepsilon'(c)$ is the relative permittivity at the low-frequency limit (excluding the effects of the EDL and a constant-phase element,

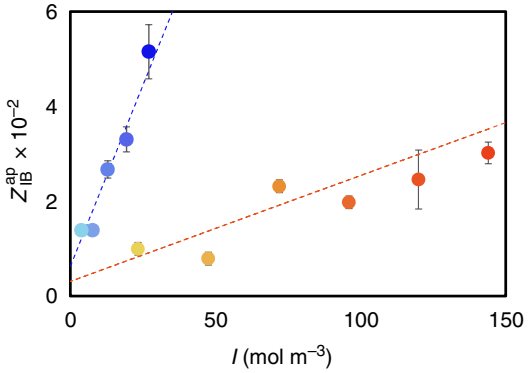

Fig. 3 Hydration states of $K_8(Si_4L_6)$ and $K_{12}(Ga_4L_6)$ cages. Hydration number Z_{IB}^{ap} plotted as a function of stoichiometric ionic strength I for $K_{12}(Ga_4L_6)$ (red and orange points, $R^2 = 0.82$) and $K_8(Si_4L_6)$ cages (blue points, $R^2 = 0.81$). Error bars represent 95% confidence intervals propagated from fit parameters of C_{tot} and G_{tot}. Each point was calculated from a set of broadband distributed circuit parameters shown in Fig. 2

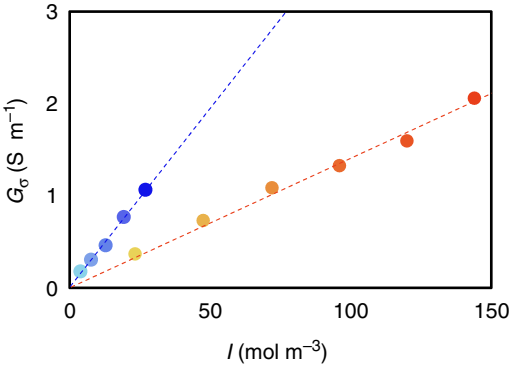

Fig. 4 Ionic conductivity of $K_{12}(Ga_4L_6)$ cages and $K_8(Si_4L_6)$ cages. Ionic conductivity plotted as a function of stoichiometric ionic strength I for $K_{12}(Ga_4L_6)$ (red and orange points, $R^2 = 0.99$) and $K_8(Si_4L_6)$ cages (blue points, $R^2 = 0.99$). Error bars represent 95% confidence intervals (smaller than point size). Each point was calculated from a set of broadband distributed circuit parameters shown in Fig. 2

see the Methods for more details) for a sample of cages with concentration c, $\varepsilon'(0)$ is the relative permittivity of DI water, $c_s^o(0)$ is the analytical concentration of water molecules (5.55×10^4 mol/m^3 at 25 °C), and $C_w(c)$ and $C_w(0)$ are the capacitive contributions of the water-loss relaxation in the cage and DI water samples, respectively[30]. To calculate the number of water molecules displaced by the volume of the cage, we estimated the volume of a cage in solution to be ~(321 ± 82) Å^3 or ~(10.7 ± 2.8) water-molecule equivalents for both $K_{12}(Ga_4L_6)$ and $K_8(Si_4L_6)$ cages) by including a solvation layer (see the Methods section). We subtracted the molar volume of the cages from $c_s^o(0)$ to determine the average number of irrotationally bound water molecules to the cage surface. Previous hydration studies found that potassium ions are not hydrated in solution[31]. Hence, we attributed all irrotationally bound water molecules to the interior and exterior of the cage.

To calculate the true hydration number Z_{IB} of the cages, we first accounted for the effect of the EDL on the apparent hydration number Z_{IB}^{ap} (Fig. 3). The electrode geometry used in these measurements produced electric fields concentrated on the surface of the electrode, and these measurements are sensitive to changes in the charge distribution of the EDL[24]. The calculated Z_{IB}^{ap} values (calculated from Eq. (1) are approximately linearly dependent on concentration in this regime. To calculate the true hydration number Z_{IB}, we applied a linear fit incorporating propagated errors in Z_{IB}^{ap}[32] and used the value at infinite dilution (Z_{IB})[20]. The error bars extracted on these fits included propagated errors from all the fit parameters included in the calculation of Z_{IB}.

We found that the $K_{12}(Ga_4L_6)$ cage is less hydrated than the $K_8(Si_4L_6)$ cage with estimated Z_{IB} values at infinite dilution of 20.4 ± 5.5 and 52.7 ± 5.5 water molecules for $K_{12}(Ga_4L_6)$ and $K_8(Si_4L_6)$ cages, respectively. Using a spherical water model and a tetrahedral approximation for the cages[33], we estimate that the number of water molecules required to make a complete hydration shell are ~50–70 for both the $K_8(Si_4L_6)$ and $K_{12}(Ga_4L_6)$ cages. This calculation suggests that the $K_{12}(Ga_4L_6)$ cages have only partial hydration shells, while the $K_8(Si_4L_6)$ cages are almost fully hydrated. This result contrasts with salt solutions, where larger charge is strongly correlated with higher hydration. A possible reason for this difference could be the presence of additional ion-paired K + ions on the K12(Ga4L6), which would block water-binding sites and reduce the charge of the multi-ion species, making water binding less energetically favorable. More strongly hydrated salts tend to have lower overall solubilities, and this trend holds true for the cages as well, where $K_8(Si_4L_6)$ has a lower solubility in water than the $K_{12}(Ga_4L_6)$ cages[34]. The steeper slope of Z_{IB}^{ap} (Fig. 3) for $K_8(Si_4L_6)$ cages further supports the conclusion that the $K_8(Si_4L_6)$ cage is more hydrated, as the larger hydrated cages would extend the thickness of the EDL and increase the EDL-related systematic error. For a deeper understanding of the environment of the cages in solution, we analyzed (below) complementary physical parameters associated with the ion pairing and ionic conductivity in solution.

Ionic conductivity of $K_8(Si_4L_6)$ and $K_{12}(Ga_4L_6)$. The bulk-fluid conductance due to ions G_σ was leveraged to compare the cages in solution to Debye–Hückel theory of simple electrolytes. For both cages, G_σ varied linearly with both ionic strength I (Fig. 4) and concentration c (Supplementary Fig. 4). This result agrees with Debye–Hückel predictions for a strong, fully dissociated electrolyte at low concentrations. However, while the overall ionic strengths measured in this experiment are low compared with conductivity studies of simple electrolyte solutions, the solutions were close to the limit of solubility of the cages in water. At high concentrations of cages, we did not observe the deviations from linearity predicted by Debye–Hückel theory, which predicts that conductivity is proportional to the square root of the ion concentration[25]. One explanation is that the concentrations required for these deviations to be detectable within our measurements could not be reached due to solubility limits of the cages. $K_{12}(Ga_4L_6)$ had a smaller slope as a function of ionic strength as well as absolute concentration c (Supplementary Fig. 4) than $K_8(Si_4L_6)$, indicating a lower overall mobility per charge in solution. This result indicates that the more charged $K_{12}(Ga_4L_6)$ cage is binding more ions to reduce the effective concentration of free ions in solution. This finding agrees with the DFT calculations that predict similar DFT energies between the charged vertex for two counterions for the $K_{12}(Ga_4L_6)$ cage versus a single counterion for the $K_8(Si_4L_6)$ cage. The lower ionic conductivity of the $K_{12}(Ga_4L_6)$ cages in conjunction with the lower hydration state suggests that the $K_{12}(Ga_4L_6)$ environments in solution could result in different equilibrium ion-pair types, and we further validated this hypothesis with the analysis of the ion-pairing relaxations.

Ion pairing of K8(Si4L6) and K12(Ga4L6). We observed a single ion-pairing relaxation for both cages with magnitude C_{IP} (Fig. 5). The magnitude of the dipolar contribution increased with ionic

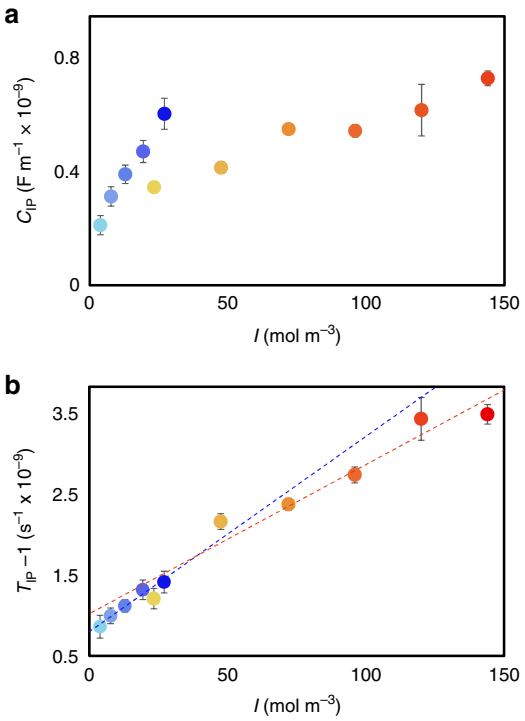

Fig. 5 Ion-pairing relaxation fit and relaxation times. Ion-pairing relaxation fit parameters of $K_{12}(Ga_4L_6)$ cages and $K_8(Si_4L_6)$ cages. **a** Dipolar contribution of ion pairs C_{IP} as a function of stoichiometric ionic strength I for $K_{12}(Ga_4L_6)$ cages (red and orange points) and $K_8(Si_4L_6)$ cages (blue points). **b** Relaxation times of ion pairs τ_{IP} as a function of stoichiometric ionic strength I for $K_{12}(Ga_4L_6)$ cages (red and orange points, $R^2 = 0.94$) and $K_8(Si_4L_6)$ cages (blue points, $R^2 = 0.97$). Error bars on both plots represent 95% confidence intervals. Each point was calculated from a set of broadband distributed circuit parameters shown in Fig. 2

strength, and—considering that we expect C_{IP} to be 0 F/m when I is 0 mMol—the relationship between C_{IP} and I appeared to be nonlinear. Dielectric spectroscopy studies of highly charged lanthanide salts (La^{3+} and Eu^{3+} salts) displayed multiple relaxations, indicating a thermal equilibrium of multiple types of ion pairs (contact and solvent-separated ion pairs)[20]. In contrast, we observed a single relaxation in the highly charged cage system, and fits allowing for multiple ion pairs converged on the same relaxation frequency and did not improve overall goodness of fit.

The presence of a single relaxation indicates that the vertices of the cages could be treated as distinct (though potentially correlated) ion-pairing sites. We did not treat the cage as a single anionic point charge because this implies that highly anionic species (12^- and 8^-) have a single, highly favored counterion-pairing state. Because ion pairs are the product of stepwise additions of ions (Fig. 1c), the presence of a single ion-pairing state within the sensitivity of our measurement implies that a particular pairing reaction step has a dramatically more favorable free energy of formation than any other step. Multiple Debye relaxations consistent with multi-step ion-pairing processes are seen in atomic salts carrying 3^+ charges, indicating that treating the cage as a highly anionic point charge with a single relaxation is unreasonable[20,35]. In contrast, treating each vertex as an independent anionic charge with steric effects from the surrounding organic ligands would account for the presence of a single, dominant ion pair in each cage. This treatment is consistent with previously untested assumptions that the distribution of charge in both the $K_8(Si_4L_6)$ and $K_{12}(Ga_4L_6)$ cages is localized to the vertices.

The capacitance C_{IP} of the ion-pair relaxation (Fig. 5) represents the dipolar contribution of the ion pairs to the overall relative permittivity of the solution. The magnitude of C_{IP} can be related to the concentration of ion pairs $[c_{IP}]$:

$$[c_{IP}] = \frac{(\varepsilon' + (1-\varepsilon')A_{IP})}{\varepsilon'} \times \frac{3k_B T\varepsilon_0}{N_A} \times \frac{1}{\mu_{eff}^2} k_{geom} C_{IP} \quad (8)$$

Here, ε' is the permittivity of the solution, A_{IP} is the shape factor of the ion pair (1/3 for a spherical approximation), k_B is the Boltzmann constant, T is the temperature, ε_0 is the permittivity of free space, N_A is the Avogadro constant, μ_{eff} is the effective dipole moment of the ion pair[30], and k_{geom} is a geometric factor relating the measured capacitance with the dielectric constant of the fluid (see Methods). The effective dipole moment μ_{eff} is:

$$\mu_{eff} = \sqrt{g}\frac{\mu_{IP}}{(1-\alpha_{IP}f_{IP})} \quad (9)$$

where μ_{IP} is the true dipole moment of the ion pair, α_{IP} is the polarizability of the dipole, f_{IP} is the reaction field factor, and g is the Kirkwood correlation factor[35]. To a first approximation, we assume that $\frac{\sqrt{g}}{(1-\alpha_{IP}f_{IP})}$ is similar in magnitude for both cages due to their similar chemistries and structures. The nonlinearity of C_{IP} (decreasing slope at higher I) could not be fully accounted for with the nonlinearity in $[c_{IP}]$ ($\frac{A_{IP}}{\varepsilon'}$ varies by ~1.3% among all cage samples) and implies a nonlinear relationship between the concentration of cages and paired counterions.

Comparing ion-pair dynamics. The $K_8(Si_4L_6)$ cage displayed larger C_{IP} values than the $K_{12}(Ga_4L_6)$ cage, both as a function of ionic strength and concentration. This C_{IP} result implies that either the $K_8(Si_4L_6)$ cage–ion pair has a much higher concentration in solution ($[c_{IP}]$), or that the dipole moment is larger for the $K_8(Si_4L_6)$ case, despite a smaller charge on the metal site. A high concentration of the $K_8(Si_4L_6)$ cage–ion pair is unlikely, due to the lower number of counterions in solution, and the higher ionic conductivity as a function of concentration. Rather, we infer a larger dipole moment, not originating from a change in charge but through a different pairing mechanism (e.g., a differently solvated pair or a different number of bound ions, Fig. 1c, d). Complementary work on $K_{12}(Ga_4L_6)$ cages by use of a combination of NMR, UV/vis spectroscopy, and ITC has previously characterized the association of large ammonium guests and counterions to the cage exterior via contact ion pairs, as those techniques are unable to detect K^+ ion-pair interactions[12]. These findings agree with our Z_{IB} and G_σ data, which also suggest that the $K_{12}(Ga_4L_6)$ forms contact ion pairs, albeit with potassium counterions rather than large, strongly bound ammonium ions. The larger C_{IP} values of $K_8(Si_4L_6)$ suggest that solvent–ion pairs should be considered in this case.

One test to determine the type of ion pair in the $K_8(Si_4L_6)$ cage is to compare two methods of calculating the association constant K_a from the measured data. If the association constants computed with these two methods disagree for a candidate type of ion pair, then the candidate is inconsistent with the measurements. The association constant can be related to $[c_{IP}]$ as follows:

$$K_a = \frac{[c_{IP}]}{[\text{cage charge sites}][K^+]} = \frac{[c_{IP}]}{(4[c]-[c_{IP}])(P\times[c]-[c_{IP}])} \quad (10)$$

where P is the number of potassium ions per cage [12 for $K_{12}(Ga_4L_6)$, 8 for $K_8(Si_4L_6)$]. A table of candidate-pairing mechanisms and the association constants computed with this method is provided in Supplementary Table 1. K_a can also be

related to the rate constants of the reaction:

$$K_a = \frac{k_1}{k_{-1}} \quad (11)$$

where k_1 and k_{-1} are the formation and decay rates of the ion pair (k_{CIP}, k_{SIP}, k_{2SIP}, etc.), respectively.

The formation and decay rates of the ion pair can be estimated from the ion-pairing time constant τ_{IP}. The time constant τ_{IP} is defined by:

$$\frac{1}{\tau_{IP}} = \frac{1}{\tau_{or}} + \frac{1}{\tau_{ch}} \quad (12)$$

where τ_{or} is the re-orientation time constant of the ion pair, and τ_{ch} is the chemical relaxation rate:[18,29,36]

$$\frac{1}{\tau_{ch}} = k_{-1} + k_1\left(M_{cage}[c] - 2[c_{IP}]\right) \quad (13)$$

and M_{cage} is the multiplier associated with each cage type (12 for $K_8(Si_4L_6)$, 16 for $K_{12}(Ga_4L_6)$). If $[c]>>[c_{IP}]$, then the equation becomes:

$$\frac{1}{\tau_{ch}} = k_{-1} + k_1\left[M_{cage}[c]\right] \quad (14)$$

In addition to helping us estimate rate constants, the τ_{IP} measurements allowed us to test for the presence of multiple types of ion pairs and transitions between different types of ion pair. A linear relationship between I and $\frac{1}{\tau_{ch}}$ indicates that the detected relaxation represents a single ion-pairing type. In contrast, a change in slope as a function of ionic strength would indicate a transition from 1-solvent ion pair to 1-contact ion pair, for example[18,29,37]. We used the slope of the linear fit to estimate the formation rate k_1, [$(1.06 \pm 0.10) \times 10^6$ mMol/s and $(1.53 \pm 0.29) \times 10^6$ mMol/s for the $K_{12}(Ga_4L_6)$ and $K_8(Si_4L_6)$ cages, respectively]. These formation rates are slightly smaller than those observed in simple salt solutions, and very fast on the timescale of a large guest or substrate association and reaction[2,38,39]. This indicates that, indeed, most ion-pairing interactions are rapid pre-equilibria to supramolecular phenomena.

The higher formation rate of the $K_8(Si_4L_6)$ cage further supported the argument that the $K_8(Si_4L_6)$ and $K_{12}(Ga_4L_6)$ cages form distinct ion-pairing species. Because the $K_8(Si_4L_6)$ cage carries lower overall charge than the $K_{12}(Ga_4L_6)$ cage, we expect a higher formation rate in the $K_{12}(Ga_4L_6)$ cages. However, this difference can be explained by multi-ion complexes such as a 2-contact ion-pair configuration, where the binding of an additional K^+ ion reduces the overall charge. The intercepts of the linear fits were approximately an order of magnitude lower than typical salt solutions ($(1.12 \pm 0.10) \times 10^9$ and $(0.93 \pm 0.11) \times 10^9$ for the $K_{12}(Ga_4L_6)$ and $K_8(Si_4L_6)$ cages, respectively). A reasonable explanation is that the re-orientation rate of the ion pair is greatly reduced by the larger mass of the cage and produces a smaller overall value of $\frac{1}{\tau_{or}} + k_{-1}$. Both cages have similar intercepts within the uncertainty of the fit, and we conclude that the decay rate and re-orientation dynamics of both ion pairs are similar.

Using the τ_{IP} data in Fig. 5b, we found that the ion-pair formation and decay rates of $K_8(Si_4L_6)$ and $K_{12}(Ga_4L_6)$ were quite similar within the uncertainty of the measurements, resulting in a relative association rate ($\frac{K_a(Ga)}{K_a(Si)}$ from Eq. S7) of approximately 0.35. This, in comparison with the estimates from Supplementary Table 1, suggests that the ion pairs measured in the $K_8(Si_4L_6)$ system have more solvent molecules than the $K_{12}(Ga_4L_6)$ ion pair to yield $\frac{\mu^2_{eff}(Si)}{\mu^2_{eff}(Ga)} > 1$. Complementary analysis of $K_{12}(Ga_4L_6)$ suggests the presence of contact ion pairs in solution for bulkier counterion chemistries, and we conclude that 2-contact ion pairs are likely present in this system due to the low solvation state and ionic conductivity of the $K_{12}(Ga_4L_6)$ cage[12]. The single hydration shell calculated for the $K_8(Si_4L_6)$ cages suggest a 1-solvent shared ion pair, while the relative K_a values suggest a 2-solvent pair to best match the K_a values from the formation and decay rates (Supplementary Tables 1, 2, and Supplementary Fig. 5). We note that the discrepancies in these calculations may be due to the simplistic models used to construct the vertex dipole moments. We also note that in order to develop more sophisticated models, one would need data from measurement techniques that—like microwave microfluidics—probe steric and solvent effects in solutions.

Discussion

In this report, we demonstrated the electrical detection of ion-pairing interactions in two metal–organic cages by microwave microfluidics. These findings are necessary for a complete understanding of charged supramolecular catalysts, as they shed light into the fast pre-equilibria of supramolecular phenomena. Our measurements demonstrate that both cages possess a single concentration-dependent Debye-type dielectric relaxation, which we attributed to ion-pairing at the vertices of the cage. We found that, unexpectedly, the $K_8(Si_4L_6)$ cage is more hydrated in solution than its more charged counterpart $K_{12}(Ga_4L_6)$. In addition, the differences in ionic conductivity and DFT binding energies between the cages support the presence of a multi-ion complex (2-contact ion pair) in the $K_{12}(Ga_4L_6)$ cage. The differences in ion-pair capacitance suggest solvent-separated ion pairs (1- or 2-solvent ion pair) in the $K_8(Si_4L_6)$ cages. Studying ion-pairing interactions is critical to understanding fundamental solution dynamics in supramolecular systems and developing design parameters for noncovalent interactions in solution. We found that broadband electrical characterization with microwave microfluidics can provide fresh insights into ion-pairing interactions in complex chemical systems, offering a new tool for characterization of supramolecular catalysts. These microwave microfluidic measurements have the potential to elucidate the direct impacts of solvation and ion-pairing on guest molecule association and enzyme-like catalysis. To achieve this, our work highlights the need to couple microwave microfluidics measurements and advanced computational models that explicitly account for charge-based, entropic, and solvent effects.

Methods

Preparation of cage samples. The $K_{12}(Ga_4L_6)$ and $K_8(Si_4L_6)$ cages were prepared and isolated according to literature procedures[2]. A stock solution of $K_{12}(Ga_4L_6)$ was prepared at ~10 mM, which was accurately calibrated by ^{1}H NMR. The calibration was performed by mixing a 100-µL aliquot of the stock solution with a 500-µL aliquot of D_2O containing 5 mM sodium tosylate as an internal standard. From this accurate concentration, serial dilutions were performed to obtain aqueous samples of $K_{12}(Ga_4L_6)$, which were then sealed under vacuum in glass ampules until measured.

The relatively low solubility of $K_8(Si_4L_6)$ in pure water limited the concentration regime which could be measured. To maximize the concentration of $K_8(Si_4L_6)$, a 35-mg cage sample was suspended in 1 mL of degassed water, sonicated for 1 h, then allowed to stand overnight. The resulting cloudy solution was centrifuged, and the supernatant was filtered with a 0.2-micron syringe filter. This saturated stock solution was calibrated by ^{1}H NMR. The calibration was performed by mixing a 100-µL aliquot of the stock solution with a 500-µL aliquot of D_2O containing 5 mM of sodium tosylate as an internal standard. From this concentration, serial dilutions were performed to obtain aqueous samples of $K_8(Si_4L_6)$, which were then sealed under vacuum in glass ampules until measured.

Unless otherwise noted, all reactions were carried out in oven-dried glassware sealed with rubber septa under a nitrogen atmosphere with Teflon-coated magnetic stir bars. Solvents were degassed by rigorous sparging with N_2 for 1 h or more. Deuterated solvents were purchased from Cambridge Isotope Laboratories. All other reagents were purchased from Sigma Aldrich and Fischer Scientific and were used as directly received without further purification. Proton nuclear magnetic

resonance (^{1}H NMR) spectra were taken with AV-300, AVB-400, AVQ-400, AV-500, DRX-500, or AV-600 Bruker spectrometers operating at 300 MHz, 400 MHz, 500 MHz, or 600 MHz.

Determination of cage parameters. Cage volumes: The volumes of the $K_{12}(Ga_4L_6)$ and $K_8(Si_4L_6)$ cages are variable due to their flexibility and motion in solution[40]. Because these structures are ideally tetrahedral, a reasonable range for their volumes was calculated from the crystallographically determined edge length (the Ga–Ga and Si–Si distances, respectively) as the lower bound for cage volume and the edge length + 0.24 nm as the upper bound.

Ionic radii of the charge centers: The treatment of each cage vertex with the hard sphere model requires the assignment of a charge value and radius. Ga(III)–triscatecholates and Si(IV)–triscatecholates are tri- and dianionic, respectively, due to the six anionic coordinating oxygen atoms and the intrinsic cationic character of Ga(III) and Si(IV). Structures derived from single-crystal X-ray diffraction measurements support the coordination environment of Ga(III)–catecholates and Si(IV)–catecholates features the symmetric octahedral arrangement of the six oxygen atoms about the cationic core. Therefore, a reasonable value for such radii can be obtained from the smallest sphere which encompasses the cationic core and the six oxygen atoms (Supplementary Fig. 6). The radius for this sphere can be calculated as the sum of the average M–O bond distance and the ionic radius of anionic oxygen. M–O bond distances were obtained from high quality Ga(III)-triscatecholate[41] and Si(IV)-enterobactin[42] model complexes due to their higher resolution relative to our host diffraction data, although those numbers agree well with previous cage datasets[40]. The ionic radius of anionic oxygen was obtained from the literature.[43]

Computational methods. All Kohn–Sham DFT calculations were performed using ORCA[44]. All structures were optimized at the B3LYP/ma-def2-SVP (B3LYP:[45]) level using D3 dispersion with Becke–Johnson damping (D3BJ dispersion:[46]). We performed vibrational frequency analysis to determine that all geometries were minimum energy stationary points. Free energy contributions were calculated using the ideal gas, rigid rotor, and harmonic oscillator approximations.

Device fabrication. The device fabrication for the microwave microfluidics devices is described in detail elsewhere[24,47,48]. We fabricated two separate types of chips: a test chip containing all microfluidic devices (Supplementary Fig. 1) and a reference chip containing bare coplanar waveguide devices (CPWs) for calibration. All devices were co-fabricated on 500-µm-thick fused silica wafers (7.62-cm diameter). Metal for CPWs was deposited by electron beam evaporation [Ti(5 nm)/Au (500 nm)]. All CPW structures were designed with 50-µm-wide center conductors, 5-µm-wide gaps and 200-µm-wide ground planes.

In addition to CPWs of different lengths, series resistors, series capacitors, and short-circuited reflects were fabricated on the reference chip. The series resistor consisted of a 10-µm × 10-µm-wide strip of Ti (1.5 nm)/PdAu(11 ± 0.5 nm) with measured direct-current resistance of ~50 Ohms. The series capacitor was identical in geometry to the series resistor, with the exception that the resistive material was omitted. The short-circuit reflects consisted of a region of conductor spanning the ground planes, gaps and center conductor, connected to a short length of transmission line on either side.

We designed devices with two-layer microfluidic channels consisting of ~50 µm of SU-8 photoresist, covered with an upper channel layer (~50 µm) of patterned polydimethylsiloxane (PDMS). The SU-8 microfluidic channels were ~80-µm wide, and exposed lengths of CPW directly to the fluid (0.5 mm, 0.66 mm, 1.32 mm, 1.98 mm, and 3.13 mm). We chose the CPW gap width and SU-8 channel height so that the electromagnetic fields primarily interacted with fluids and SU-8 rather than the PDMS layer. An acrylic press bar screwed into an aluminum chuck clamped the PDMS block to the chip.

We measured the CPWs on a manual microwave probe station using a vector network analyzer (VNA). We measured the complex S-parameters as a function of frequency and acquired 640 frequency points from 40 kHz to 110 GHz on a log frequency scale, at an RF power level of −15 dBm (where 0 dBm corresponds to a power of 1 mW), and with an intermediate frequency (IF) bandwidth of 10 Hz. All measurements were performed on a temperature-controlled stage programmed to 25 °C. The chips and aluminum blocks were kept on the stage for a minimum of 5 min after the stage reached the desired temperature to ensure thermal equilibration. After measurements were performed on the reference and empty test devices, fluid was injected into the channels and held for at least 2 min at zero flow rate prior to fluid measurements.

We determined the measured S-parameters of the distributed circuit parameters for each transmission line segment using the calibration techniques described elsewhere (calibrated S-parameters in Supplementary Fig. 7)[24,46–48]. We performed a two-tier calibration consisting of a reference chip and the microfluidics fluid-loaded chip. For the first-tier calibration, we measured S-parameters for seven different bare CPW lengths (0.420 mm, 1.000 mm, 1.735 mm, 3.135 mm, 4.595 mm, 7.615 mm, and 9.970 mm), a series resistor, a series capacitor, and a short-circuit reflect. We first performed a multiline thru-reflect-line (TRL)[49] calibration to determine the propagation constant of the bare-CPW lines (γ_0), followed by the series-resistor calibration[50] to compute the capacitance per unit length of the bare CPW section (C_0). In the second-tier calibration, we measured four transmission lines, as well as a single short-circuit reflect structure loaded with fluid on the test chip. We then performed multiline TRL calibration and series resistor calibrations with a de-embedding procedure to obtain the propagation constant for the microfluidic channels (γ_{tot}). The propagation constant for the bare CPW lines can be written as:

$$\gamma_0 = \sqrt{(R_0 + i\omega L_0)(G_0 + i\omega C_0)}, \tag{15}$$

where ω is the angular frequency and R_0, L_0, G_0, and C_0 are the distributed resistance, inductance, conductance, and capacitance per unit length of the bare-CPW lines, respectively, as a function of frequency. We assumed that the conductivity of fused silica is negligible (G_0=0), and the materials in the CPW devices are non-magnetic. These assumptions allowed us to derive R_0 and L_0 from the reference chip, and relate them to the propagation constant of a fluid-loaded line:

$$\gamma_{tot} = \sqrt{(R_0 + i\omega L_0)(G_{tot} + i\omega C_{tot})} \tag{16}$$

The multiline TRL calibration on the microfluidic test chip allowed us to relate the propagation constant of the fluid directly to the capacitance G_{tot} and conductance C_{tot} for frequencies in the range 1 GHz–110 GHz. For lower frequency measurements, we utilized the series resistor calibration and de-embedded our raw measurements to the fluid-loaded portion of the line by accounting for the effect of cables, probes, and the CPW sections leading up to the fluid.[48,51] For every measurement set, we first measured air and de-ionized water in the channels to establish baseline levels for C_{tot} and G_{tot} for known fluid properties.

Fitting the EDL. We describe the effect of the EDL as operating in series with the admittance of the fluid for fluids with dissolved ions. The EDL can be modeled as a Cole–Cole relaxation (see Supplementary Fig. 2 for circuit diagram):

$$Y_{EDL} = Y_{CPE} + G_{EDL} + i\omega C_{EDL} = Y_{CPE} + i\omega \frac{C_{EDL}}{1 + (i\omega\tau_{EDL})^{1-\alpha_{EDL}}} \tag{17}$$

where C_{EDL} is the capacitance associated with the EDL, α_{EDL} is a shape-broadening parameter and, τ_{EDL} is the characteristic relaxation time associated with the formation of the EDL under electric field. The conductance and capacitance of the EDL (G_{EDL} and C_{EDL}, respectively) are in parallel with the constant-phase element Y_{CPE}:

$$Y_{CPE} = Q\omega^{-n} e^{i\frac{\pi}{2}n} \tag{18}$$

where Q and n are fitting parameters, and where Q has the units [Sm^{-1} Hz^n]. We fix $n = -1$ because the concentration of ions is low in the sample, and allowing n to vary did not change the fit parameters.

Fitting Y_{tot}. We simultaneously fit log(C_{tot}) and log(G_{tot}) from 60 kHz to 60 GHz, and C_w and G_w+G_σ for the frequency range 3 GHz–25 GHz, with fit parameters and functions normalized to be approximately one. The inclusion of C_w and G_w+G_σ into the fitting model was necessary to address the collinearity between G_σ and CPE effects in the model. We varied the frequency range over the full frequency spectrum (40 kHz–110 GHz) to minimize the error in the fit parameters. The frequency range from 60 kHz to 60 GHz minimized the uncertainty in the fit parameters. We found that a minimum frequency range of 1 MHz–50 GHz was necessary to accurately describe the ion pairing at all concentrations. This frequency range is not general and depends on the ionic mobility and EDL dynamics of the specific system.

The fit of the EDL admittance Y_{EDL} and corresponding data (Supplementary Fig. 8b, f), allow us to extract the bulk-fluid admittance. The bulk-fluid properties contain the water relaxation Y_w as well as the fluid conductance G_σ, where the fit and corresponding data are pictured in Supplementary Fig. 8c and g. The relaxation magnitude of Y_{IP} (Supplementary Fig. 8d, h), is on the order of 10^{-11} F/m, roughly two orders of magnitude smaller than the water relaxation. Including the ion-relaxation peak was necessary to produce symmetric (Cole–Cole) relaxations for the EDL and resulted in overall lower residuals across the high-frequency regime (see Supplementary Fig. 9 for comparison of residuals).

Constructing estimates of relative binding constants. We construct independent estimates of the relative association constants of the $K_{12}(Ga_4L_6)$ and $K_8(Si_4L_6)$ cages from the measurements of τ_{IP} and C_{IP} to extract information about the ion-pairing types. From the C_{IP} data, we can use an empirical square-root fit ($C_{IP} \propto \sqrt{I}$) to relate the $C_{IP}(Ga)$ to $C_{IP}(Si)$ ($C_{IP}(Si)$=1.9$C_{IP}(Ga)$), and include this relationship to get the relative concentrations of ion-pairing c_{IP}:

$$\frac{[c_{IP}(Ga)]}{[c_{IP}(Si)]} = \frac{\frac{(\varepsilon'(Ga)+1-\varepsilon'(Ga))A_{IP}}{\varepsilon'(Ga)} \times \frac{1}{\mu^2_{eff}(Ga)} C_{IP}(Ga)}{\frac{(\varepsilon'(Si)+1-\varepsilon'(Si))A_{IP}}{\varepsilon'(Si)} \times \frac{1}{\mu^2_{eff}(Si)} C_{IP}(Si)} \approx \frac{\mu^2_{eff}(Si)}{1.9 \times \mu^2_{eff}(Ga)}. \tag{19}$$

We then use this relationship to relate the association constants:

$$\frac{K_a(Ga)}{K_a(Si)} = \frac{[c_{IP}(Ga)]}{(4[c]-[c_{IP}(Ga)])(12[c]-[c_{IP}(Ga)])} \times \frac{(4[c]-[c_{IP}(Si)])(8[c]-[c_{IP}(Si)])}{[c_{IP}(Si)]}. \quad (20)$$

In the limit $c_{IP} \ll c$, where the ion pairs are assumed to have similar correlation factors and reaction fields (see Eq. (9)), we merge Eq. (19) into Eq. (20):

$$\frac{K_a(Ga)}{K_a(Si)} \approx \frac{\mu_{eff}^2(Si)}{1.9 \times \mu_{eff}^2(Ga)} \times \frac{32}{48} = 0.35 \frac{\mu_{eff}^2(Si)}{\mu_{eff}^2(Ga)}. \quad (21)$$

We calculated relative dipole moments for contact and solvent-separated ion pairs for $K_8(Si_4L_6)$ and $K_{12}(Ga_4L_6)$ (see Supplementary Table 2) from our estimates of the effective ionic radii of the cage charge centers (see Supporting Information). In calculating the dipole moment, we assumed the ion-pair pivot point as the edge of the cage charge complex, due to the much greater mass of the cage. We also tabulated relative free energies of each combination of ion-pairing type (Supplementary Table 1, Supplementary Fig. 4).

Data availability

The data that support the findings of this study are available from the corresponding author upon reasonable request.

Received: 4 April 2019 Accepted: 16 April 2019
Published online: 17 May 2019

References

1. Yoshizawa, M., Klosterman, J. K. & Fujita, M. Functional molecular flasks: new properties and reactions within discrete, self-assembled hosts. *Angew. Chem. Int. Ed.* **48**, 3418–3438 (2009).
2. Hong, C. M. et al. Deconvoluting the role of charge in a supramolecular catalyst. *J. Am. Chem. Soc.* **140**, jacs.8b01701 (2018).
3. Hart-Cooper, W. M. et al. The effect of host structure on the selectivity and mechanism of supramolecular catalysis of prins cyclizations. *Chem. Sci.* **6**, 1383–1393 (2015).
4. Cullen, W., Misuraca, M. C., Hunter, C. A., Williams, N. H. & Ward, M. D. Highly efficient catalysis of the kemp elimination in the cavity of a cubic coordination cage. *Nat. Chem.* **8**, 231–236 (2016).
5. Evans, N. H. & Beer, P. D. Advances in anion supramolecular chemistry: from recognition to chemical applications. *Angew. Chem. Int. Ed.* **53**, 11716–11754 (2014).
6. Grommet, A. B. & Nitschke, J. R. Directed phase transfer of an $Fe^{II}_4 L_4$ cage and encapsulated cargo. *J. Am. Chem. Soc.* **139**, 2176–2179 (2017).
7. Yi, S., Brega, V., Captain, B. & Kaifer, A. E. Sulfate-templated self-assembly of new M_4L_6 tetrahedral metal organic cages. *Chem. Commun.* **48**, 10295 (2012).
8. Rizzuto, F. J., Wu, W., Ronson, T. K. & Nitschke, J. R. Peripheral templation generates an $M(II)_6L_4$ guest-binding capsule. *Angew. Chem.* **128**, 8090–8094 (2016).
9. Bruns, C. J. et al. Emergent ion-gated binding of cationic host-guest complexes within cationic $M_{12}L_{24}$ molecular flasks. *J. Am. Chem. Soc.* **136**, 12027–12034 (2014).
10. Bolliger, J. L., Ronson, T. K., Ogawa, M. & Nitschke, J. R. Solvent effects upon guest binding and dynamics of a $Fe^{II}_4L_4$ cage. *J. Am. Chem. Soc.* **136**, 14545–14553 (2014).
11. Custelcean, R. Anion encapsulation and dynamics in self-assembled coordination cages. *Chem. Soc. Rev.* **43**, 1813–1824 (2014).
12. Sgarlata, C. et al. Different and often opposing forces drive the encapsulation and multiple exterior binding of charged guests to a M_4L_6 supramolecular vessel in water. *Chem. - A Eur. J.* **23**, 16813–16818 (2017).
13. Tobey, S. L. & Anslyn, E. V. Studies into the thermodynamic origin of negative cooperativity in ion-pairing molecular recognition. *J. Am. Chem. Soc.* **125**, 10963–10970 (2003).
14. Valderrey, V., Escudero-Adán, E. C. & Ballester, P. Highly cooperative binding of ion-pair dimers and ion quartets by a bis(Calix[4]Pyrrole) macrotricyclic receptor. *Angew. Chem. Int. Ed.* **52**, 6898–6902 (2013).
15. Sambrook, M. R. et al. Anion-templated assembly of pseudorotaxanes: importance of anion template, strength of ion-pair thread association, and macrocycle ring size. *J. Am. Chem. Soc.* **127**, 2292–2302 (2005).
16. Pluth, M. D., Tiedemann, B. E., van, H. H., Nunlist, R. & Raymond, K. N. Diffusion of a highly charged supramolecular assembly: direct observation of ion association in water. *Inorg. Chem.* **47**, 1411–1413 (2008).
17. Schalley, Christoph A., ed. *Analytical methods in supramolecular chemistry*. Vol. 1. (John Wiley & Sons, 2012).
18. Buchner, R., Capewell, S. G., Hefter, G. T. & May, P. M. Ion-pair and solvent relaxation processes in aqueous Na_2SO_4 solutions. *J. Phys. Chem. B* **103**, 1185–1192 (1999).
19. Wachter, W. et al. Is there an anionic Hofmeister effect on water dynamics? Dielectric spectroscopy of aqueous solutions of NaBr, NaI, $NaNO_3$, $NaClO_4$, and NaSCN. *J. Phys. Chem. A* **109**, 8675–8683 (2005).
20. Friesen, S. et al. Hydration and ion association of La^{3+} and Eu^{3+} salts in aqueous solution. *Phys. Chem. Chem. Phys.* **20**, 8812–8821 (2018).
21. Basey-Fisher, T. H. et al. Microwave Debye relaxation analysis of dissolved proteins: towards free-solution biosensing. *Appl. Phys. Lett.* **99**, 10–13 (2011).
22. Ermilova, E., Bier, F. F. & Hölzel, R. Dielectric measurements of aqueous DNA solutions up to 110 GHz. *Phys. Chem. Chem. Phys.* **16**, 11256 (2014).
23. Tros, M. et al. Picosecond orientational dynamics of water in living cells. *Nat. Commun.* **8**, 1–7 (2017).
24. Little, C. A. E. et al. Modeling electrical double-layer effects for microfluidic impedance spectroscopy from 100 KHz to 110 GHz. *Lab Chip* **17**, 2674–2681 (2017).
25. Wright, M. *An Introduction to Aqueous Electrolyte Solutions*. (Wiley, Hoboken, NJ, 2007).
26. Jeong, J. Y. et al. Is fast relaxation water really a free water? *2017 42nd Int. Conf. on Infrared, Millimeter, and Terahertz Waves*, (IRMMW-THz). IEEE, 2017.
27. Chekalin, N. V. & Shakhparonov, M. I. The mechanism of dielectric relaxation in water. *J. Struct. Chem.* **9**, 789–790 (1968).
28. Bazant, M. Z., Thornton, K. & Ajdari, A. Diffuse-charge dynamics in electrochemical systems. *Phys. Rev. E - Stat. Nonlinear, Soft Matter Phys.* **70**, 1–24 (2004).
29. Buchner, R., Samani, F., May, P. M., Sturm, P. & Hefter, G. Hydration and ion pairing in aqueous sodium oxalate solutions. *ChemPhysChem* **4**, 373–378 (2003).
30. Cavell, E. A. S. Dielectric relaxation in non aqueous solutions. *Trans. Faraday Soc.* **67**, 2225 (1971).
31. Chen, T., Hefter, G. & Buchner, R. Dielectric spectroscopy of aqueous solutions of KCl and CsCl. *J. Phys. Chem. A* **107**, 4025–4031 (2003).
32. Little, C. A. E. et al. Modeling electrical double-layer effects for microfluidic impedance spectroscopy from 100 KHz to 110 GHz. *Lab Chip* **17**, 2674–2681 (2017).
33. York, D., Evensen, N. M., Martínez, M. L., De Basabe Delgado, J. Unified equations for the slope, intercept, and standard errors of the best straight line. *Am. J. Phys.*, **72**, 367–375 (2004).
34. Buchner, R. & Hefter, G. Interactions and dynamics in electrolyte solutions by dielectric spectroscopy. *Phys. Chem. Chem. Phys.* **11**, 8984 (2009).
35. Hünenberger, P. & Reif, M. *Single-Ion Solvation: Experimental and Theoretical Approaches to Elusive Thermodynamic Quantities*. (Royal Society of Chemistry, London, UK, 2011).
36. Schrödle, S., Wachter, W., Buchner, R. & Hefter, G. Scandium sulfate complexation in aqueous solution by dielectric relaxation spectroscopy. *Inorg. Chem.* **47**, 8619–8628 (2008).
37. Buchner, R. & Barthel, J. Kinetic processes in the liquid phase studied by high-frequency permittivity measurements. *J. Mol. Liq.* **63**, 55–75 (1995).
38. Barthel, J., Kleebauer, M. & Buchner, R. Dielectric relaxation of electrolyte solutions in acetonitrile. *J. Solut. Chem.* **24**, 1–17 (1995).
39. Levin, M. D. et al. Scope and mechanism of cooperativity at the intersection of organometallic and supramolecular catalysis. *J. Am. Chem. Soc.* **138**, 9682–9693 (2016).
40. Pluth, M. D. & Raymond, K. N. Reversible guest exchange mechanisms in supramolecular host-guest assemblies. *Chem. Soc. Rev.* **36**, 161–171 (2007).
41. Borgias, Brandan A., et al. Structural Chemistry of Gallium (II1). Crystal Structures of K3 [Ga (catecholate) 3)]· 1.5 H2O AND [Ga (benzohydroxamate) 3]· H2O· CH3 CH2OH. *J. Coord. Chem.* **15**, 109–123 (1986).
42. Baramov, T. et al. Synthesis and structural characterization of hexacoordinate silicon, germanium, and titanium complexes of the E. coli siderophore enterobactin. *Chem. - A Eur. J.* **19**, 10536–10542 (2013).
43. Shannon, R. D. Revised effective ionic radii and systematic studies of interatomic distances in halides and chalcogenides. *Acta crystallographica section A: crystal physics, diffraction, theoretical and general crystallography* **32**, 751–767 (1976).
44. Neese, F. The ORCA program system. *Wiley Interdiscip. Rev. Comput. Mol. Sci.* **2**, 73–78 (2012).
45. Becke, A. D. Density-functional thermochemistry. III. The role of exact exchange. *J. Chem. Phys.* **98**, 5648–5652 (1993).
46. Grimme, S. et al. Effect of the damping function in dispersion corrected density functional theory. *J. Comput. Chem.* **32**, 1456–1465 (2011).
47. Ma, X. et al. A Multistate Single-Connection Calibration for Microwave Microfluidics. *IEEE Trans. Microw. Theory Tech.* **66**, 1099–1107 (2018).

48. Booth, J. C. et al. Quantitative permittivity measurements of nanoliter Liquid volumes in microfluidic channels to 40 GHz. *IEEE Trans. Instrum. Meas.* **59**, 3279–3288 (2010).
49. Liu, S. et al. Hybrid Characterization of Nanolitre Dielectric Fluids in a Single Microfluidic Channel Up to 110 GHz. *IEEE Trans. Microw. Theory Tech.* **65**, 5063–5073 (2017).
50. Williams, D. F., Wang, C. M. & Arz, U. An optimal multiline TRL calibration algorithm. *IEEE MTT-S Int. Microw. Symp. Dig.* **3**, 1819–1822 (2003).
51. Williams, D. F. & Walker, D. K. Series-Resistor Calibration. in 50th ARFTG Conference Digest 131–137 (1997).

Acknowledgements

The authors would like to thank Aaron Hagerstrom and Edward Garboczi for their helpful feedback. Certain commercial equipment, instruments, or materials are identified in this paper to specify the experimental procedure adequately. Such identification is neither intended to imply recommendation or endorsement by the National Institute of Standards and Technology nor is it intended to imply that the materials or equipment identified are necessarily the best available for the purpose. This paper is an official contribution of NIST; not subject to copyright in the US.

Author contributions

A.C.S. made, calibrated, and analyzed microwave microfluidics measurements. C.M.H. prepared and characterized metal–organic cages. M.C.G. performed DFT calculations. C.A.E.L. fabricated the microwave microfluidic chip. J.C.B., N.D.O., R.G.B., K.N.R., K.A.S., F.D.T. and C.J.L. contributed to interpretation, analysis, and preparation of the paper.

Additional information

Supplementary information accompanies this paper at https://doi.org/10.1038/s42004-019-0157-9.

Competing interests: The authors declare no competing interests.

Reprints and permission information is available online at http://npg.nature.com/reprintsandpermissions/

Publisher's note: Springer Nature remains neutral with regard to jurisdictional claims in published maps and institutional affiliations.